



Geometric controls on flat slab seismicity

Dan Sandiford^{a,b,c,*}, Louis Moresi^{a,d}, Mike Sandiford^a, Ting Yang^{e,a}

^a School of Earth Sciences, University of Melbourne, Australia

^b Institute of Marine and Antarctic Studies, University of Tasmania, Australia

^c German Research Center for Geosciences – GFZ-Potsdam, Germany

^d Australian National University, Australia

^e Southern University of Science and Technology, China

ARTICLE INFO

Article history:

Received 10 April 2019

Received in revised form 10 July 2019

Accepted 23 August 2019

Available online xxxx

Editor: B. Buffett

Keywords:

subduction

intermediate depth earthquakes

flat slabs

bending

ABSTRACT

The relationship between intraslab seismicity and the dynamics of subduction is a subject of ongoing debate. Uncertainty surrounds (1) the extent to which the stress regime associated with slab earthquakes reflects the driving/resisting forces of subduction, or more localised processes such as metamorphic or thermo-elastic volume change, and (2) the relative contribution of uniform (stretching/shortening) and flexural (bending/buckling) deformation modes in slabs. Because variations in slab curvature are very clear in subduction zones with flat slab segments, such settings allow for assessment of the relationship between slab geometry, bending and seismicity. Using a numerical model that reproduces published flat slab geometries we show how bending rates, which are dominated by the advective component, relate to downdip curvature gradients. Based on published slab geometries, we show that the patterns of seismicity in the Peruvian and Mexican flat slabs, vary systematically with slab curvature gradient. Seismicity is restricted to regions colder than about 600 °C. This means that only the upper half of flat slab bending zones are expressed seismically, providing the appearance of a uniform extensional regime.

© 2019 Elsevier B.V. All rights reserved.

1. Introduction

Intermediate depth earthquakes generated within subducting slabs offer important insights into dynamic and metamorphic processes involved with lithospheric recycling. However, with seismic activity strongly heterogeneous both within and between slabs (Isacks and Molnar, 1971; Fujita and Kanamori, 1981; Chen et al., 2004; Bailey et al., 2009), developing a consistent petrological and dynamic framework for slab seismicity is an ongoing challenge. The nucleation of slab earthquakes requires not only a state of differential stress, but also significant fault strength reduction. At intermediate depths (50–300 km) the dehydration of hydrous minerals is thought to provide the required strength reduction (Peacock, 2001). The exponential depth decay of slab seismicity (Kirby et al., 2013), together with earthquake clustering at appropriate inferred P – T conditions, provides strong signals for the role of dehydration (Hacker et al., 2003; Yamasaki and Seno, 2003). In contrast, the relationship between slab earthquakes, various sources of differential stress and the dynamics of subduction remains less clear (Hacker et al., 2003).

The connection between slab seismicity and subduction dynamics has been the subject of many previous studies (e.g. Isacks and Molnar, 1971; Engdahl and Scholz, 1977; Wang, 2002; Myhill, 2012), and the idea that intraslab seismicity reflects modes of large-scale, buoyancy-driven deformation within the slab is common (e.g. Fujita and Kanamori, 1981; House and Jacob, 1982). The classic studies of Isacks and Molnar (1969, 1971) established the influential paradigm that slab earthquake orientations mainly reflect uniform stress/strain modes. In this view slabs with shallow extent, or significant gaps between intermediate and deep earthquakes, exhibit downdip tension/stretching (DT) due to negative buoyancy with respect to the asthenosphere, i.e. the slab pull force (Forsyth and Uyeda, 1975). In contrast, slabs with deep and continuous seismicity are argued to undergo downdip compression/shortening (DC) as a result of resistance from the lower mantle.

Moment tensor eigenvector distributions often show a high degree of homogeneity, characterising many slabs as DT or DC-type (e.g. Isacks and Molnar, 1969; Bailey et al., 2009). Yet intermediate depth seismicity is also widely observed to be distributed in two bands within the slab, often with opposing focal mechanism styles (Engdahl and Scholz, 1977; Brudzinski et al., 2007). These double seismic zones (DSZs) are usually expressed between 50–300 km depth, are separated by 20–40 km and appear to merge downdip (Peacock, 2001; Wei et al., 2017). The focal mechanisms

* Corresponding author at: Institute of Marine and Antarctic Studies, University of Tasmania, Australia.

E-mail address: dan.sandiford@utas.edu.au (D. Sandiford).

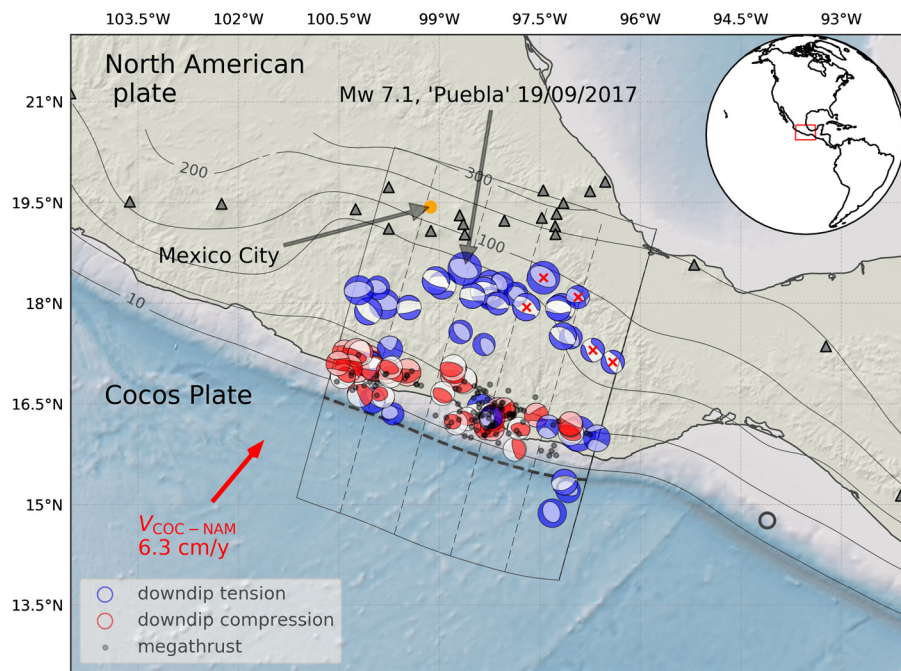


Fig. 1. Mexican flat slab region. Beachballs show lower-hemisphere projected CMT moment tensors, for intraslab events. Red shows down-dip compressional (DC) events, blue for down-dip tensional (DT). Black circles show inferred megathrust events. Black solid lines show depth contour of the Slab2 model (Hayes et al., 2018) at [10, 30, 60, 100, 200, 300] km. Black dashed lines show the azimuth along which Slab2 data is sampled to produce a region-averaged slab surface geometry (actual sample lines are spaced at 10 km). Red crosses show inferred intraslab earthquakes that lie above the Slab2 model. Triangles show active volcanoes. (For interpretation of the colours in the figure(s), the reader is referred to the web version of this article.)

associated with DSZs typically show that the upper part of the slab mantle is in down-dip compression while the lower part down-dip tension, consistent with unbending in the presence of dehydration embrittlement (Engdahl and Scholz, 1977; Wang, 2002; Sleep, 1979).

However, because some DSZs continue beyond the expected depths of unbending, additional sources of stress have been argued to play a significant role (Fujita and Kanamori, 1981). Other studies propose that DSZs primarily represent a metamorphic/dehydration phenomena, rather than the dynamics of unbending (Peacock, 2001). Significant complexity will be expected when mechanical and metamorphic conditions contribute variably to the stress state (Wang, 2002). Disentangling the signal of mechanical stress linked to the forces that drive/resist subduction, from the effects of dehydration, as well as more localised stress sources therefore remains an ongoing challenge.

In most subduction settings slabs bend near the outer rise, and unbend beneath the forearc and mantle wedge. Beyond this, they often maintain a relatively uniform dip for several hundred kilometers before they begin to interact with the transition zone (England et al., 2004). However some slab segments, such as those attached to the Cocos and Nazca plates, show more complicated geometries characterized by a prominent intermediate depth flat slab section. This geometric complexity will clearly be associated with additional zones of slab bending. If bending does exert a significant control on slab stress, and if earthquakes reflect the stress state associated with bending/unbending, flat slabs should offer a prospective setting to observe these relationships.

While recent studies have help explain the dynamic evolution of flat slabs (Manea and Gurnis, 2007; Schepers et al., 2017), the controls on seismicity within flat slabs remains less well understood. For example, Kumar et al. (2016) attributed extensional focal mechanisms in the southern Peruvian flat slab (referred to here as the PFS) to buoyancy forces associated with slab pull, as has been commonly invoked for slab seismicity along much of the eastern Pacific margin (Comte et al., 1999). In contrast, Melgar et al. (2018)

propose that the damaging 2017 Puebla earthquake in the Mexican flat slab was a bending-related earthquake because of the correlation between slab geometry (a region of moderate curvature) and focal mechanism (DT). A rupture like this would be expected for the upper part of a curved elasto-brittle sheet with convex-up shape. However, much of the historical intermediate depth seismicity in the Mexican flat slab is located in the flat slab segment, where curvature is low (as can be seen in Fig. 3).

In this study we reexamine the relationship between slab seismicity and slab geometry in the Mexican and Peruvian flat slabs. We begin by reviewing the seismic expression of prominent flat slabs based on historical earthquake catalogues. Results from a numerical visco-plastic simulation of flat slab subduction are then presented. Strain rates in this model are dominated by bending, with the primary component of this bending being due to the advection of the slab through finite curvature gradients (termed the advective bending rate). It is this specific mode of deformation which we highlight as a potential control on the distribution and orientation of seismicity in flat slab settings. The relationship is explored by comparing the slab seismicity with the slab geometry, specifically the estimated down-dip slab curvature gradient. Following previous studies, we suggest that slab temperature also plays a key role, strongly inhibiting seismicity in deeper parts of the slab. In young slabs this restricts seismicity to the upper half of the bending zones. Together, bending rates and temperature effects give rise to the characteristic expression of alternating segments of DC and DT ruptures [e.g. Kawakatsu, 1986]. We briefly speculate on the applicability of this framework to other slab segments along the eastern Pacific margin.

2. Study regions

This paper focuses on parts of the Mexico and Peru flat slabs, shown in Fig. 1 and Fig. 2. There are two primary considerations in selection the specific analysis regions. The first is that there is no active buoyant-ridge. The second consideration represents a balance between choosing slab segments that are large enough to

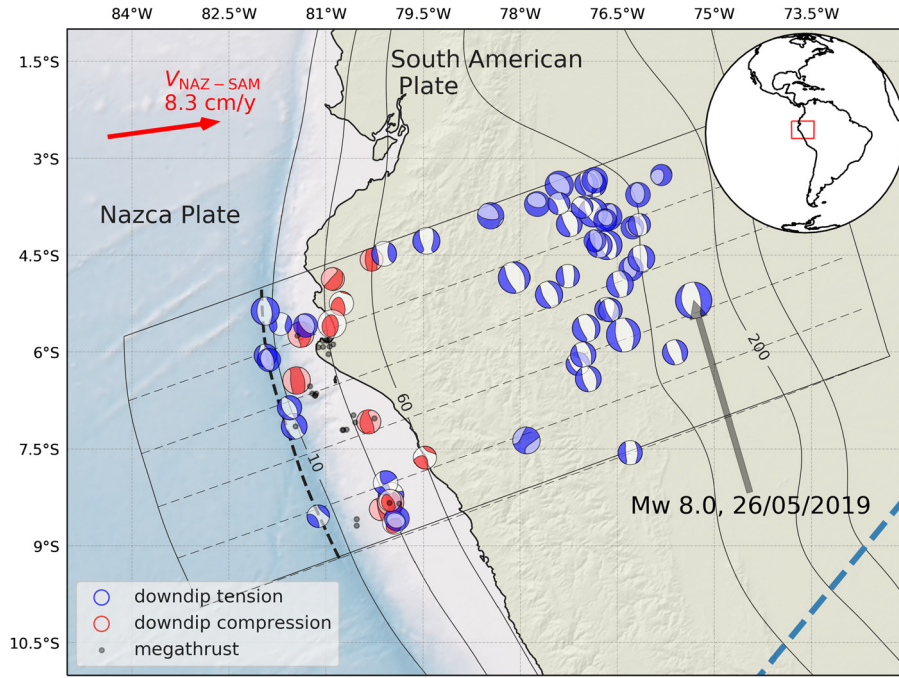


Fig. 2. Peru flat slab region. CMT moment tensor symbology follows Fig. 1. Black lines show depth contour of Slab2 model. Black dashed lines show the azimuth along which Slab2 data is sampled to produce a region-averaged slab surface geometry. The Nazca ridge is being subducted at the southern edge of the region, represented by the blue dashed line. Deep slab seismicity (>400 km) is not shown.

include a significant number of slab earthquakes, while also having a relatively strong morphological similarity along strike. This similarity is important as it enables us to link the patterns in seismicity, aggregated across the domains, to the geometric features of the slab.

The Mexican flat slab (MFS) underlies parts of southern Mexico, where the Cocos plate is subducting under the North America plate at around 6 cm/yr. The MFS region shown in Fig. 1 has a trench parallel width of about 440 km. The trench perpendicular length of the flat slab is about 150 km (Manea et al., 2017). The oceanic Moho of the flat slab lies at only ~ 45 km depth (Kim et al., 2013), suggesting partial delamination of the upper plate mantle lithosphere. The tectonic evolution of the MFS is enigmatic as there is no actively subducting buoyant anomaly (aseismic-ridge or oceanic plateau) to act as a trigger (Manea et al., 2013). Seismicity within the flat slab occurs at epicentral distances of less than 100 km from Mexico City, which therefore poses significant hazard, exemplified by the 2017 Mw 7.1 Puebla Earthquake. The contours depicted in Fig. 1 show the recently published Slab2 slab surface model (Hayes et al., 2018). There is some inconsistency between the Slab2 model for the MFS and the earthquake data we use in this study. As shown in the map in Fig. 1, near the north-east limit of the MFS a number of flat slab earthquakes are shallower than the Slab2 model. In Section 3 we discuss this inconsistency in more detail.

The Peruvian flat slab (PFS) is significantly larger than the MFS, both in terms of its trench parallel (>1000 km) and trench perpendicular flat slab extent (>300 km) (Manea et al., 2017). The oceanic Moho of the subducted PFS, as determined by receiver functions, lies at around 80 km depth (Bishop et al., 2017) significantly deeper than in the MFS. The subduction of the Nazca Ridge is likely to be a contributing factor to flat subduction as well as the cessation of arc volcanism since ~ 3 Ma. The Nazca Ridge is currently subducting along the southern edge of the PFS. The approximate northern limit of the ridge is shown with the blue dashed line in Fig. 2. The seismic expression of the southern part of the PFS is likely to be influenced by Nazca Ridge subduc-

tion, while that influence is expected to reduce towards the north (Kumar et al., 2016). Based on these considerations we only consider the northern half of the PFS in this study. The total width of the PFS study region (shown in Fig. 2) is about 480 km.

3. Data and processing

3.1. Earthquake data

The accuracy of teleseismic-determined hypocenters varies considerably with location technique, seismograph distribution, and hypocenter depth (e.g. Jackson, 1980; Engdahl et al., 1998; Craig, 2019). The approach we take to integrating available global earthquake datasets is informed by several factors: (1) if only teleseismic P and S wave travel times are used, depth errors may be several tens of km errors, due to fact that the origin time of an earthquake trades off against its focal depth (Jackson, 1980); (2) The use of depth phases means that depth uncertainty can be reduced to around 10–15 km, with epicentral uncertainties likely to be similar (Engdahl et al., 1998); (3) For shallow earthquakes (<50 km), where the depth phases overlap with P wave coda, agency-reported depth phases are likely to be less accurate (Engdahl et al., 1998); (4) depth errors in the CMT database can be significantly higher than the best available global travel time data (Craig, 2019).

A simple way of addressing these issues is to combine the comprehensive CMT focal mechanism database (Ekström et al., 2012) with the hypocenters from the ISC-EHB database. The ISC-EHB location procedure uses depth phases, via the EHB algorithm (Engdahl et al., 1998), to minimise uncertainties in depth. In all cases where a CMT event has a corresponding ISC-EHB entry, we use hypocenter information from the latter. If there is no ISC-EHB record, we retain the CMT hypocenter, identifying these events in relevant figures. We will refer to the combined set of hypocenters/moment tensors as the CMT-ISC data. As we only use events with a CMT record, the data is assumed to have the same completeness level and duration as CMT database. From 2004, the CMT catalogue is complete to Mw 5.0, while the earlier data, extending to 1976, are complete to 5.4 (Ekström et al., 2012).

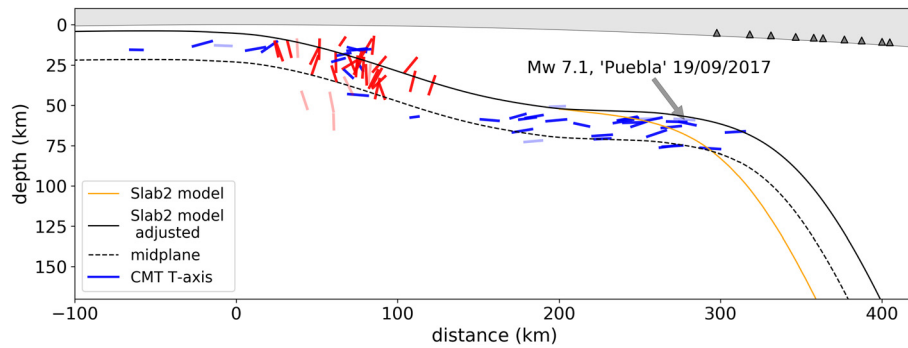


Fig. 3. Mexican flat slab seismicity. Projection of CMT-ISC events on a vertical cross-section, along the azimuth shown with dashed lines in Fig. 1. T-axes with a greater transparency level show events where no ISC-EHB hypocenter is available. Earthquakes are coloured according to the same scheme as in Fig. 1, red: DC, blue: DT. Yellow line shows the original Slab2 model (region-averaged). Solid black line shows the adjusted surface based on Slab2, discussed in main text. Dashed line shows the midplane, which is an orthogonal projection of the surface, and will be used to calculate slab curvature/(gradients). Grey region shows the earth surface.

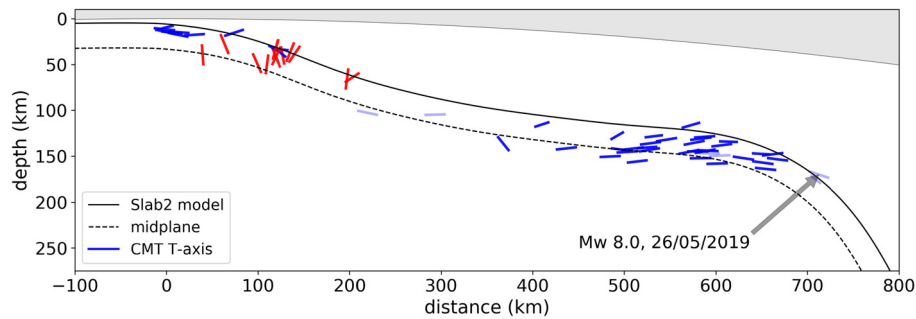


Fig. 4. Northern Peru flat slab seismicity. Projection of CMT-ISC events on a vertical cross-section, along the azimuth shown with dashed lines in Fig. 2. Other symbology follows Fig. 3.

For events occurring in the flat slabs, we assume that the incorporation of reliable depth phases, as utilised in ISC-EHB, leads to typical depth errors around 10–15 km. While this is not sufficient to conclusively rule out the presence of DSZs in either of the flat slabs, we do not see any separation of hypocenters. The recent study of Florez and Prieto (Florez and Prieto, 2019), which incorporates depth phases within double-difference relocation framework, does not identify a DSZ in the northern PFS (their study does not cover the MFS region).

Earthquakes on the subduction megathrust constitute a significant proportion of the overall the seismic activity at subduction zones. Although flat slab seismicity does not overlap spatially with the megathrust, filtering of potential megathrust events is important in terms of identifying additional slab seismicity occurring up-dip from the flat slab zone. Even with improved ISC-EHB locations, hypocenter location alone does not enable us to discriminate clearly between potential megathrust and slab earthquakes. As such, we emphasise focal mechanism orientation as the primary indicator of megathrust rupture events. Further details of the procedure for identifying megathrust events are contained in Appendix A.

3.2. Slab geometry data

The geometric analysis conducted in this study requires knowledge of the slab geometry and its spatial (downdip) gradients. Like earthquake hypocenters, the 3D morphology of slabs in the upper mantle is subject to uncertainty, particularly in regions where seismicity is sparse and/or slab morphology is inherently complex. The recent Slab2 surface model (Hayes et al., 2018) uses multiple input data types to augment traditional earthquake-derived slab geometry models. For each flat slab region we define a representative slab top geometry by calculating the average value of the Slab2 model along a series of trench perpendicular lines. The lines are spaced

at approximately 10 km intervals along the trench, as shown in Fig. 1 and Fig. 2. Because the Slab2 model does not always extend to trench, we build a spline representation between the Slab2 data (region-averaged profile) and bathymetry data, providing a continuous representation of the Slab2 model that extends well into the oceanic plate. These region-averaged slab surfaces are shown with solid black lines in Fig. 3 and Fig. 4.

In examining the relationships between slab dynamics and geometry, we will refer frequently to the slab midplane. We use this term in relation to both the numerical model and observed flat slab geometries based on the Slab2 model. The notion of a midplane serves as a proxy for the neutral plane of bending, and hence as a way of analysing slab dynamics in terms of thin-sheet relationships (as discussed in Section 7.1). Of course, the actual neutral plane of bending, both in nature and in the models, is a dynamic feature which may vary with respect to a fixed reference position, for instance the slab surface. However, for our purposes, knowledge of such variability is not essential. The analysis of the numerical model in Section 7, which is based on a slab surface defined midplane, shows this approximation to the neutral plane is sufficient for understanding the key relationships between geometry and slab deformation rate.

In the numerical model a midplane is generated by seeding particles at a specified depth in the oceanic plate and advecting these with the flow, such that they track the evolving slab morphology. The position of the midplane is shown with a dashed line in Fig. 6 and Fig. 7. For the MFS and PFS we generate the midplane by an orthogonal translation of the Slab2 model, with a distance that is proportional to thermal thickness of the plate at the trench. The constant of proportionality is 0.3, consistent with estimates of how DSZ width increases with plate age (Brudzinski et al., 2007). The resulting Slab2 midplanes are shown with dashed black lines in Fig. 3 and Fig. 4. In estimating the curvature and curvature gradi-

ent of the midplane, a second order Butterworth filter is used to remove wavelengths less than 100 km.

The use of multiple input data sources in the Slab2 model is likely to improve the overall accuracy of the subduction geometry, however it may do so at the cost of some level of consistency between a specific data source (i.e. earthquake hypocenters) and the resulting slab model. This problem appears to affect the Slab2 model for the MFS, particularly in the northeast corner, where a number of flat slab earthquakes lie above the slab model (shown with red crosses in Fig. 1). Using the region-averaged Slab2 surface model as a starting model, we developed an adjusted MFS slab surface compatible with observed MFS earthquakes from the CMT-ISC data. Fig. 3 shows the original Slab2 surface with a solid yellow line and the adjusted surface as a solid black line. In this adjusted model, the majority of earthquakes in MFS cluster lie beneath the slab surface. The midplane used to calculate MFS geometric quantities is based on the adjusted model.

4. Seismic expression of flat slab segments

Cross sections showing the distribution and orientation of slab seismicity are shown in Fig. 3 (MFS) and Fig. 4 (PFS). The CMT-ISC events are represented with vectors, centered at the earthquake hypocenter. The vectors show the projection of the moment tensor T-axis onto the plane of the cross section. Note that the vector length is determined by the projected component of the T-axis, not earthquake magnitude. While the moment tensor does not uniquely determine the pre-rupture stress state, the T-axes are expected to lie within the same quadrant as the smallest stress eigenvector. A common interpretation is that the T-axes represent the orientation of most extensive co-seismic strain release (Isacks and Molnar, 1971; Bailey et al., 2009).

The distribution and orientation of seismicity in the MFS and PFS regions shows a number of similarities. Inboard from the trench, slab seismicity forms two main clusters, one in the dipping section of the slab near the trench (<100–200 km) and another cluster occurring within the flat slabs. These flat slab earthquakes extend throughout most of the flat slab in Mexico whereas they are skewed towards the distal end of the flat slab in Peru. Metamorphic dehydration has been highlighted as a possible control on the onset of seismicity at the distal end of PFS (Kumar et al., 2016).

The spatial clustering of flat slab earthquakes is also reflected in the orientation of the earthquake moment tensors. Within the flat slabs, T-axes are predominately aligned downdip, indicating a stress state of effective tension (DT). Slab earthquakes within the near-trench cluster are somewhat more variable, but generally have DC orientation, with T-axes primarily aligned perpendicular to the slab surface. These shallow slab events with downdip compressional mechanisms, have been recognised in previous studies (Lemoine et al., 2002); here we argue that they represent a simple process of slab unbending.

Throughout the MFS, the plunge of earthquake T-axes remains fairly constant and sub-horizontal. In the PFS, T-axes undergo a slight CW rotation with increasing distance from the trench. Earthquakes continue into the distal hinge, where the slab has begun to significantly steepen, an example being the recent Mw 8.0 earthquake of 26/05/2019 (labelled in Fig. 4). The fact that these distal PFS earthquakes have deeper hypocenters and steeper T-axes, suggests that the location of the distal hinge in the Slab2 surface model is a robustly constrained feature. In contrast, the fact that none of the MFS T-axes show this rotation into a distal hinge, is an indication that the Slab2 model slightly underestimates the distal extent the flat slab. Meanwhile, the Slab2 model appears to slightly under-estimate the degree of flattening in PFS, particularly at the trench-ward end of the flat slab.

5. Numerical model of flat slab subduction

In this section we provide a brief overview of a numerical model designed to investigate the dynamics of the Mexican flat slab. A more detailed description of the model is contained in B.2. The numerical model evolves according to simplified conservation equations for mass, momentum and energy within a 2D Cartesian domain. Solutions to the equations are derived using a Galerkin finite-element approximation. The domain is 1250 km in the vertical direction and has an aspect ratio of 4. The model initial conditions comprise three plates and a small slab which follows a circular arc with a curvature radius of 200 km, truncated at 150 km depth. An overview of the model domain, initial conditions and evolving boundary conditions is shown in Fig. B.11 in B.2. Previous studies have demonstrated that an imposed low viscosity mantle wedge (LVW) can cause slabs to flatten directly beneath the upper plate (Manea and Gurnis, 2007). We adopt a similar LVW strategy in this study, with further details of provided in the next section.

In the numerical model the mantle is treated as an incompressible, highly viscous fluid in which inertial forces and elastic stresses can be neglected. Thermal buoyancy helps to drive the flow in the model. The thermal variations are coupled to the momentum equation through their effect on density as well as through the temperature-dependent viscous rheology. There is no compositional difference between the subducting and upper plate (no continental crust or mantle) nor is there any compositional differentiation of the oceanic lithosphere (no oceanic crust). Mantle rheology (including oceanic lithosphere) is prescribed by a composite flow law that includes linear high-temperature creep, as well as a scalar visco-plastic approach sufficient for capturing pseudo-brittle as well as distributed plastic deformation within the slab (see B.3 for additional information).

The top surface of the model is driven by a set of evolving velocity boundary conditions, as described in B.2. It is important to point out that the development of the flat slab is not a direct consequence of these boundary conditions. Additional experiments showed slab flattening was triggered by a LVW when subduction was driven solely by slab buoyancy (no tangential velocity boundary conditions were applied). The boundary conditions are critical, however, for representing the Miocene tectonic environment of the Cocos subduction margin. In particular, the boundary conditions enforce rapid convergence velocities (particularly in the early stages of the model) as well as a short subducting plate length (via an imposed migrating ridge), which together reproduce the very young age of the present Cocos slab (~15 Ma).

5.1. Low viscosity wedge and subduction interface

The trigger for Miocene flat slab development in Central Mexico remains unclear, particularly since there are no known buoyancy anomalies on the subducting plate, as have been proposed for the Peruvian and Pampean slabs (e.g. Manea et al., 2017). Previous studies demonstrated that the introduction of a LVW could lead to the development of a flat slab, which forms mainly due to dynamic overthrusting of the upper plate (Manea and Gurnis, 2007; van Hunen et al., 2000). Following this approach, our model incorporates a LVW that lies between two arbitrary depths (45 km & 150 km), the top of the slab, and a vertical boundary given by the intersection between the slab top and lower depth limit. The wedge viscosity is 2×10^{20} Pa s, similar to the viscosity of the asthenospheric mantle in the model, but much weaker than the stagnant part of the mantle wedge that typically develops due to the strong temperature dependence of the mantle rheology (i.e. the cold corner). To generate an established convergent margin, we allowed an initial stage of subduction to proceed for 20 Myr, after which the LVW was imposed.

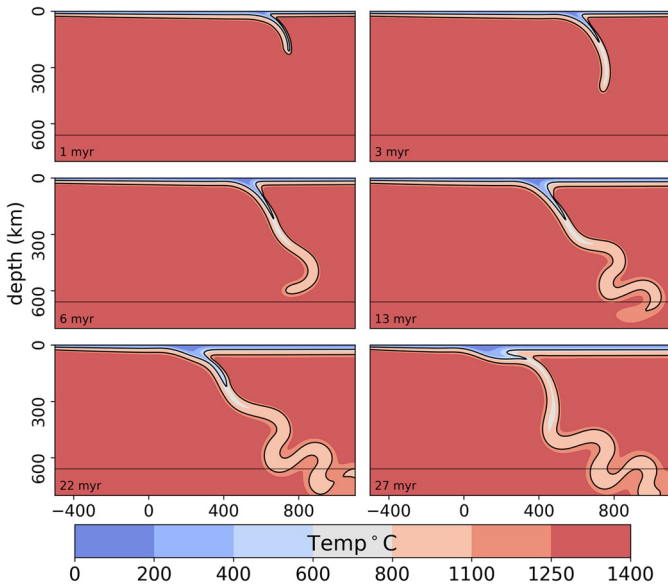


Fig. 5. Model temperature field. The panels show temperature field in a subregion of the model domain, providing an overview of the evolving slab geometry during the simulation. Slab flattening is initiated at 20 million years through a reduction in mantle wedge viscosity (as described in main text). Temperature contours (black lines) are drawn at 600 °C and 1100 °C isotherms. Horizontal black line shows 660 km, where there is an increase ($\times 5$) in mantle viscosity.

The subduction interface provides decoupling between the upper and lower plates. We use a strategy frequently employed in continuum numerical subduction models, whereby a weak layer is imposed on the top of the subducting plate, and is continuously entrained into the decoupling region. One difference in our methodology is that we constrain the minimum (7 km) and maximum thickness (14 km) of the weak subduction interface material. Further details of this approach can be found in Sandiford and Moresi (2019). The subduction interface has a constant viscosity of 9×10^{18} Pa.s. The rheology associated with the subduction interface transitions from the weak, isoviscous value towards the background mantle rheology. A depth-dependent cosine taper is used to control this transition. The onset of the cosine taper occurs at 70 km, with a vertical taper width of 30 km. Hence the rheological signature of the subduction interface material vanishes completely by 100 km depth.

6. Model results

Fig. 5 shows the evolution of the slab in the upper mantle, up to the time (27 Myr) when the total length of the flat slab is comparable to the present day MFS. A prominent feature of the model is the complex buckling that develops as the slab interacts with the viscosity jump ($\times 5$) in the transition zone, promoted by high convergence velocity in the early stages of the model. These transition zone folds are a completely unconstrained feature of the model, due to lack of clear tomographic resolution for the Cocos slab at these depths. However, the patterns of slab deformation in the transition zone do not strongly effect the deformation patterns within the flat slab, which are fundamentally controlled by the local slab geometry and subduction velocity (as we show later). Before the onset of flattening, the 600 °C isotherm extends to a depth of ~ 200 km (e.g. Fig. 5 at 13 Myr). This is similar to the maximum depth of seismicity in the Rivera slab to the west of the MFS, which has a more typical subduction morphology (Manea et al., 2017). As the model slab progressively flattens, the slab isotherms shallow. Once the slab has completely flattened, the 600 °C isotherm becomes fully confined within the flat slab domain (e.g. Fig. 5 at 27 Myr, also Fig. 6).

Due to the dynamic nature of the model we do not expect to reproduce the precise geometry of the flat slab. Nevertheless the morphology of the model (at time 27 Myr) appears to have a close correspondence to the present day MFS. This is evidenced in the consistency between the model slab thermal structure and historical seismicity, shown in Fig. 7C. When projected onto the model temperature field, using the trench as the common reference point, the majority of CMT-ISC earthquakes in the flat slab are enclosed by the 600 °C isotherm, which defines a narrow tongue within the slab. Our model supports a previous suggestion that temperature distribution inhibits seismicity beyond the distal hinge of the MFS (Manea et al., 2013). The minimum radius of curvature of the slab in our model is ~ 150 km, which occurs in the bend at the distal end of the flat slab. This is likely to be somewhat larger than the curvature radius in the current MFS, where the distal hinge of flat slab appears to have rolled back about 70 km, since 7 Ma (Ferrari et al., 2012). The numerical model does not develop this retreating hinge. By design, the model convergence velocity (6.3 cm/yr) and subducting plate age at the trench (17 Ma – with a plate thermal thickness of ~ 60 km), closely approximates the present conditions at the Middle America Trench along the segment shown in profile in Fig. 1.

Key features of the flat slab dynamics are shown in Fig. 6. The colour maps are masked so they show only the strong part of the slab (see figure caption for details). In the bottom panel of Fig. 6 we show the downdip stress component (σ_{ss}), which reveals the strong role of bending in the model dynamics. Regions of bending are characterised by quasi-symmetric lobes either side of the midplane. In the flat part of the slab, the stress above the midplane is associated with extension (–ve sign). In the regions where the flexural state changes sign, the stress eigenvectors rotate so that they appear to connect the zones of effective tension (shown in blue). We speculate that this pattern reflects the residual component of stress due to the slab pull. The magnitude of the slab pull stress, evaluated on the oceanward side of the trench, is quite low (>20 MPa). This is consistent with the majority of the slab weight being supported by drag in the mantle.

The top panel of Fig. 6 shows the magnitude of the slab strain rate (square root of the second invariant of the tensor). The strain rate magnitude shows a more localised distribution than the stress distributions (shown in the bottom two panels). This reflects the fact that the deviatoric stress saturates throughout the zones of high bending rate, such as the central part of the flat slab. Intervening regions of very low strain rate are not yielding, which is reflected in high effective viscosity, shown in the second panel of Fig. 6.

7. Analysis

7.1. Slab bending and geometry in numerical models

The model flat slab is segmented into regions of high bending rate, which are yielding, and intervening regions which have very low strain rate and are not yielding. As we show in this section, these patterns are indicative of an important geometric control on the slab bending rate. When a sheet is deformed by pure bending, the distribution of strain rate in the downdip direction ($\dot{\epsilon}_{ss}$) is a function of the curvature rate (a material derivative) multiplied by distance from the midplane (Kawakatsu, 1986; Ribe, 2001):

$$\dot{\epsilon}_{ss} = -y \frac{DK}{Dt} = -y \left(\frac{\partial K}{\partial t} + u_s \frac{\partial K}{\partial s} \right) \quad (1)$$

where s refers to a unit vector along the slab midplane, y is the distance perpendicular to the midplane, $\frac{D}{Dt}$ is the material derivative following s , K is the curvature and u_s is the velocity component parallel to the midplane. The term $u_s \frac{\partial K}{\partial s}$ is referred to as an

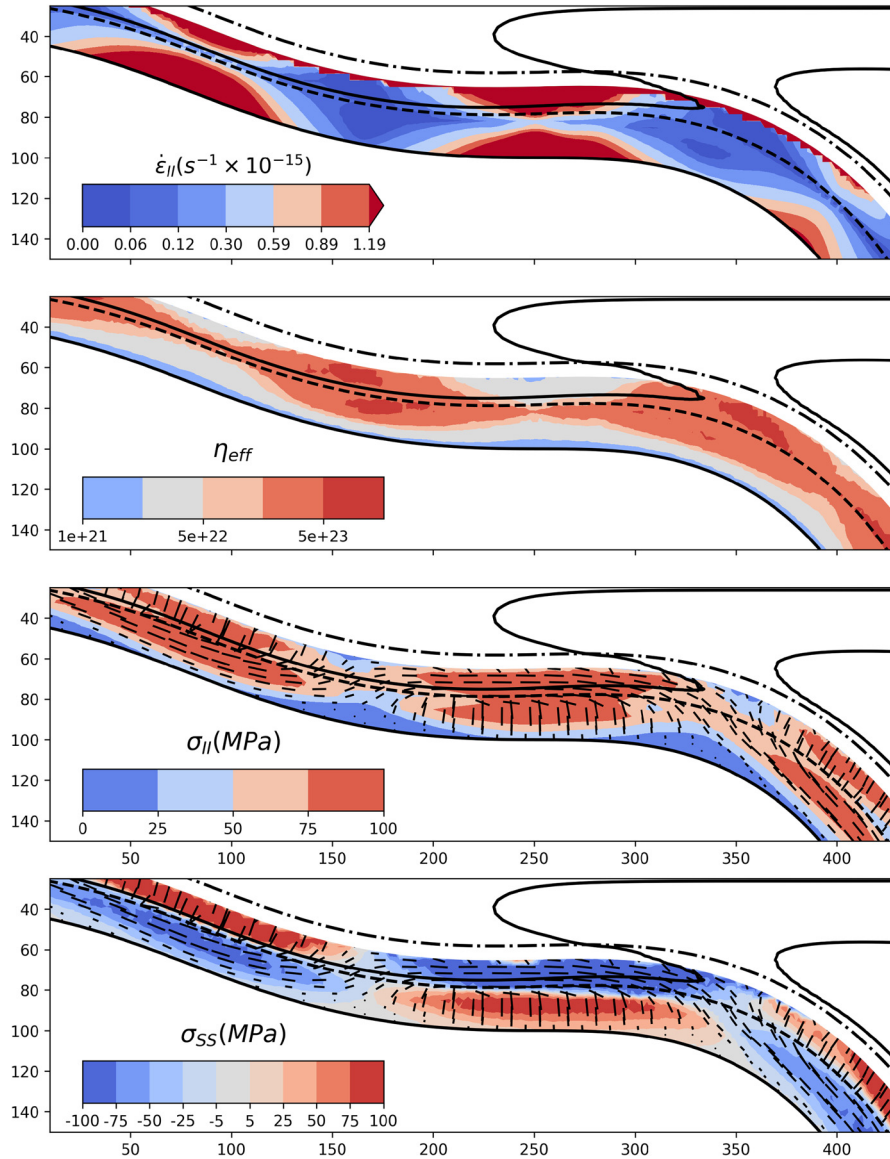


Fig. 6. Features of slab dynamics. All panels: solid lines are 600°C and 1100°C isotherms. Dashed lines is the slab midplane, dot-dashed line shows the slab top (above the subduction interface zone). Colormaps show only the strong interior part of the slab: the subduction interface zone, LVW, upper plate, and parts of the mantle are above 1100°C isotherm have been masked. Top panel: magnitude of the strain rate tensor (square root of the second invariant). Second panel: effective viscosity (log-scale). Third panel: magnitude of the deviatoric stress tensor. Black oriented line segments represent the least compressive principal stress, with length scaled by the stress magnitude. Bottom panel: downdip component of the stress tensor resolved parallel to the slab midplane.

advective bending rate. While slabs are unlikely to have a completely static geometric profile, it is expected that the advective term will dominate in the subduction hinge (Buffett and Becker, 2012).

We now explore this geometric-bending relationship in the context of our numerical model. Fig. 7b shows the downdip strain rate ($\dot{\epsilon}_{ss}$) while the top panel of the same figure (a) shows the normalised value of curvature and curvature gradient evaluated along the slab midplane. The slab midplane curvature has a quasi-harmonic variation, with characteristic truncated local maxima. The derivative induces a phase offset in the curvature gradient profile, relative to the curvature. There is a strong correlation between the curvature gradient profile ($\frac{\partial K}{\partial s}$) and the downdip strain rate distribution ($\dot{\epsilon}_{ss}$). The zones where downdip strain rates are smallest coincide with the local maxima in the curvature amplitude, where the curvature gradient is close to zero. This suggests that the advective component of the bending rate is a dominant control on the slab deformation rate.

7.2. Geometric controls on flat slab seismicity

In this section we explore whether the advective bending mode, a dominant feature of the numerical model dynamics, may be relevant for the seismic expression of the flat slabs in Mexico and Peru. We focus firstly on the spatial distribution of earthquakes (clustering) and then assess the orientation of the seismicity (focal mechanisms). In order to estimate patterns of advective bending, spatial derivatives of the slab midplane are needed. The processing of Slab2 model data, and determination of the midplane, is detailed in Section 3.

Fig. 8 shows seismicity-geometry relationships for the MFS. The top panel shows the projected T-axes on a vertical cross section, while the bottom panel shows the curvature and curvature gradient based on the slab midplane geometry. Histograms in the bottom panel reflect the spatial distribution of the seismicity (see figure caption for further details). The spatial clustering of slab earthquakes throughout the MFS region exhibits a qualitative correlation with curvature gradients determined from the Slab2 mid-

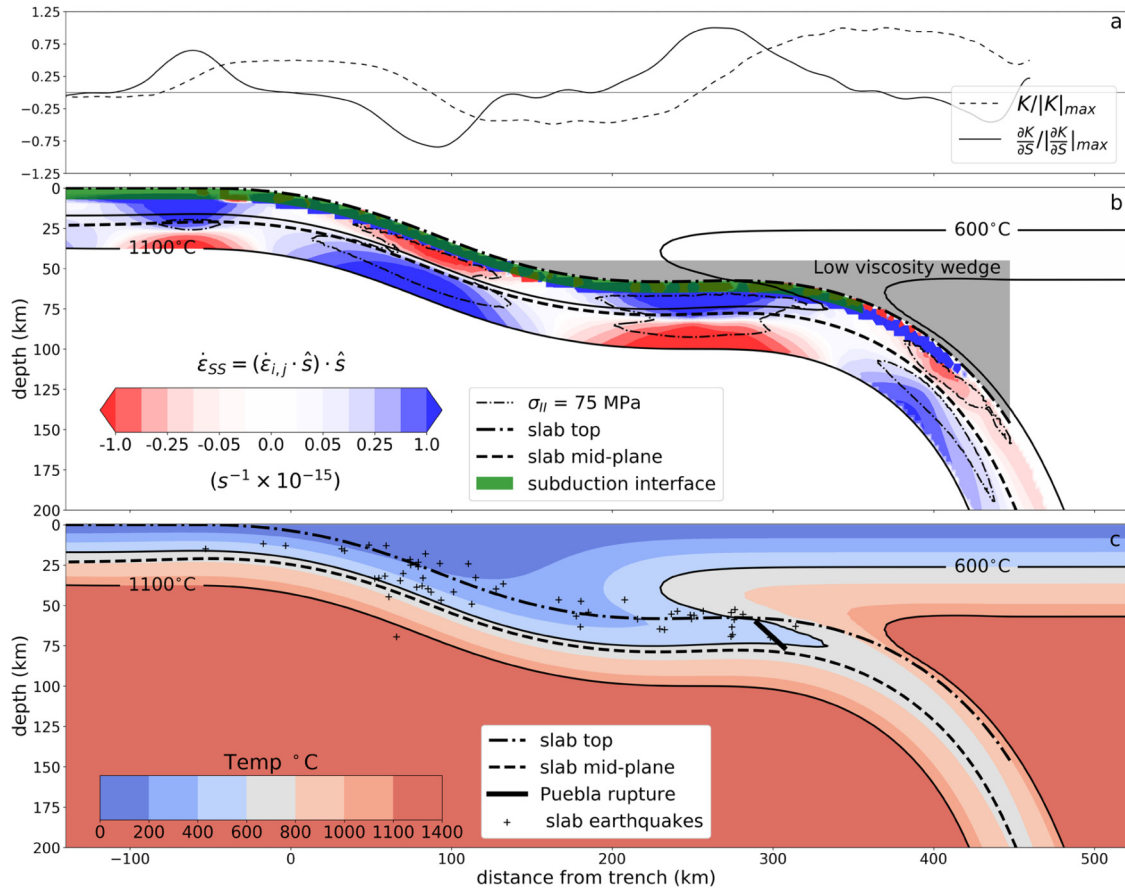


Fig. 7. Numerical model bending and thermal structure. All panels show model time of 27 Myr. a) Normalised curvature and curvature gradient of slab midplane. b) Downdip strain rate component ($\dot{\epsilon}_{SS}$) resolved parallel to the slab midplane, +ve values (blue) show zones of downdip extension, -ve values (red) are shortening. Solid black lines show 600°C and 1100°C isotherms. Dashed black line – slab midplane. Shaded green region – subduction interface. Shaded grey region – extent of the imposed low viscosity wedge. c) temperature field. Black circles – Mexican flat slab earthquake locations from CMT-ISC catalogue. Thick solid black line – projected trace of Puebla rupture from (Melgar et al., 2018).

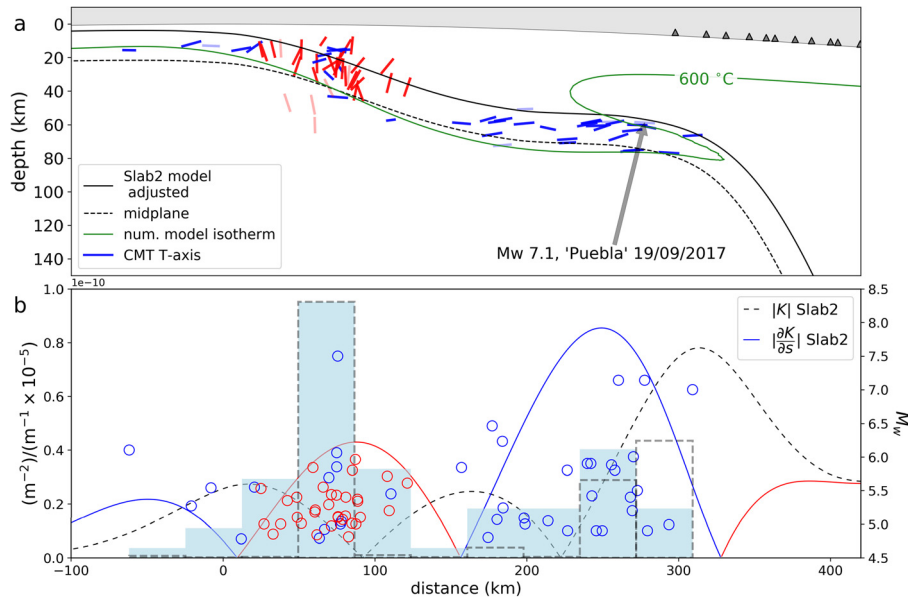


Fig. 8. MFS seismicity-geometry relationships. a) Projection of CMT-ISC events on a vertical cross-section, along the azimuth shown with dashed lines in Fig. 1. Solid black line shows adjusted Slab2 surface model (see main text and Fig. 3 for details). Dashed line shows the midplane along which curvature/(gradient) is calculated. b) Pale blue histogram, normalised seismic activity rate (number of events per bin over catalogue time). Dashed histogram, normalised moment release (cumulative energy release per bin per time). Circles – intraslab events with height corresponding to magnitude (M_w). Solid line (blue and red line) shows absolute value of the downdip slab curvature gradient. Blue represents slab sections with positive curvature gradient, which are expected to be in extension above the midplane, whereas red indicates negative curvature gradient and expected shortening above the midplane. Dashed line shows absolute value of the curvature. Both curvature gradient (m^{-2}) and curvature (m^{-1}) are plotted on the left handed axis, with the latter multiplied by 10^{-5} .

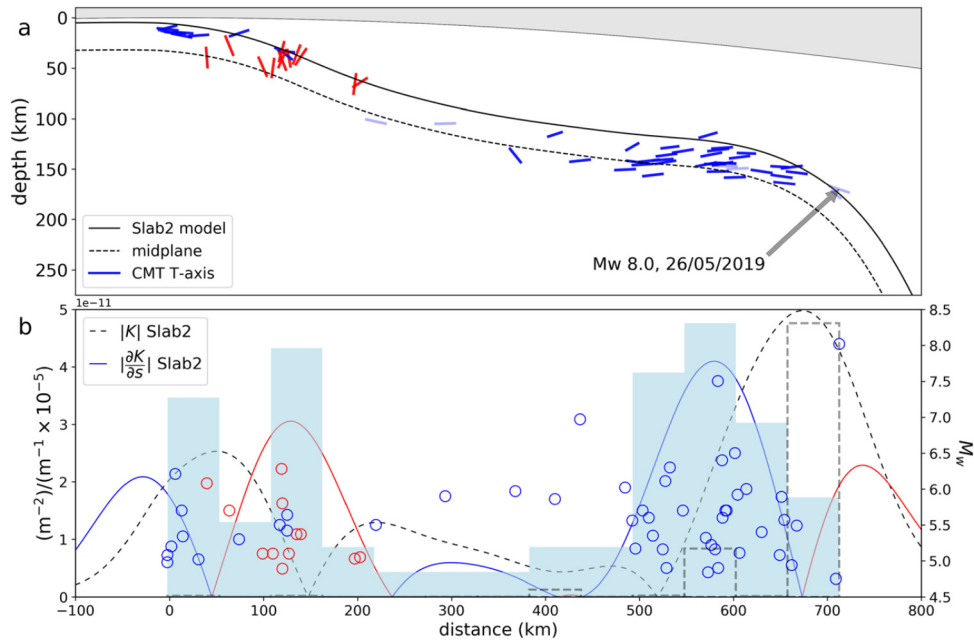


Fig. 9. Northern PFS seismicity-geometry relationships. Symbology is identical to Fig. 8.

plane. The curvature gradient predicts high bending rates within the MFS, as well as in the unbending region proximate to the trench; both correspond to regions of high seismic activity rate. Meanwhile the prominent seismic gap between these earthquake clusters coincides with low curvature gradient. Another, smaller peak in the curvature gradient occurs seaward of the trench, which is associated with a small number of outer rise events. Fig. 9 shows an equivalent analysis for the PFS. Inboard from the trench there are two dominant earthquake clusters. Like the MFS, there is clear qualitative correlation between the clustering of seismicity and the amplitude of curvature gradients based on the slab surface model. Note that the vertical scale on the LHS of Fig. 9b is half that of the MFS. The MFS has estimated peak curvature gradients almost twice as high as the PFS.

The variation in downdip slab curvature-gradient, and inferred bending rates, appears to have significant explanatory power for the distribution of seismicity within the two flat slab settings. However, if advective bending does have a causal relationship with slab seismicity, the orientation of faulting should also vary systematically with the curvature gradient. We may also expect bending zones to exhibit DSZs, with the orientation of upper and lower plane events corresponding to shortening and extension, or vice versa, depending on the sign of the bending rate. While the orientation of moment tensor T-axes does vary systematically with the curvature gradient, DZSs are not observed in the MFS or PFS. In the flat slab segments, earthquakes appear to be restricted to a single band, with DT orientations. We can reconcile the absence of DSZs, however, if only the upper half of the flat slab bending zones are seismogenic [e.g. Kawakatsu, 1986]. A simple explanation is that seismicity is usually restricted to parts of the plates/slabs that are colder than 600–700 °C (McKenzie, 1969). As shown in Fig. 7c, this critical isotherm range is expected to partition the MFS close to the neutral plane of bending, into a colder, seismogenic upper zone, and a warmer, aseismic lower zone.

8. Discussion

We have demonstrated that in two flat slab settings there are systematic correlations between the inferred bending rate and patterns of seismicity. Yet given that earthquakes represent elastic

strain release, it is important to try to reconcile why inferences about deformation rate can provide a useful proxy for distribution and rupture style of seismic energy release. To a degree, it is the existence of earthquakes themselves (or at least pervasive inelastic deformation) that underpins this relationship. As past studies have pointed out, inelastic deformation must account for much of the total strain accumulation during bending (Engdahl and Scholz, 1977; Billen, 2005). This follows from that fact that a representative elastic slab stress at peak curvature is on the order of 10 GPa, (i.e. deviatoric stress 20 km from the neutral plane of bending, using a Young's modulus of 60 GPa, and a radius of curvature of 150 Km). The yield stress of slab faults is inferred to be 1–2 orders of magnitude less than this (McAdoo et al., 1978; Kita and Katsumata, 2015). This means that in the regions of high (advective) bending rates, slabs have elasto-brittle loading/unloading cycles which are 1–2 orders of magnitude smaller than the length scales involved in bending/unbending. Importantly, because the stress can saturate so rapidly, slabs will often exhibit a flexural stress state that is different to the implied elastic stress based on the sign of the slab curvature (Engdahl and Scholz, 1977; Wang, 2002). In the limit of very weak slabs, the flexural stress state will tend to approximate the bending rate, not the curvature. Overall, the relationships highlighted in this study support previous work suggesting that slabs must yield rapidly after the onset of bending in the hinge (Engdahl and Scholz, 1977; Billen, 2005).

While the framework we propose accounts well for the broad features of flat slab seismicity, there are some isolated events which are inconsistent with the inferred bending rate (based on the region-averaged Slab2 geometry). On 26/05/2019 a Mw 8.0 earthquake occurred in the distal hinge of the northern PFS, as shown in Fig. 9. This earthquake has a DT focal mechanism, as is characteristic of all PFS earthquakes. However, based on the Slab2 model for this region, the recent event occurred slightly beyond the zone of predicted bending-related upper slab extension. With the curvature gradient at this point being negative, the slab would be expected to be undergoing unbending. Within the framework we have proposed, the simplest explanation for these events are that there is some along strike variability in the slab morphology that is not captured in the Slab2 model. Alternatively, they may also highlight a number of complexities that are being ne-

glected when we draw a simple connection between the seismicity and the curvature gradient. The advective part of the bending rate, proportional to downdip curvature gradients, provides only a partial description of slab deformation rate. A component of uniform strain rate, for instance stretching due to slab pull, is likely to also contribute. Retreat of the distal hinge relative to the upper plate, as is inferred in the MFS, could also be occurring in parts of the PFS. There is an ongoing role for geodynamic modelling to investigate the internal dynamics of slabs, with both time dependence and 3 dimensional effects being important issues for future studies to address.

In this study we examined very specific tectonic settings where prominent flat slabs are present, without the complexity of nearby buoyant-ridge subduction. We think it likely, however, that the framework presented has relevance for other regions. In other parts of the Nazca slab, like northern Chile, which may not be traditionally thought of as flat slabs, there is nevertheless a conspicuous zone of slab dip reduction beneath the arc (Engdahl et al., 1998). Although the existence of a DSZ in northern Chile remains somewhat ambiguous, the DSZ polarity (DT above DC) observed in microseismicity by Comte and Suarez (1994), is consistent with bending in a zone of positive curvature gradient. More generally, wherever such partial flattening and subsequent steepening occurs, it is reasonable to infer that positive curvature gradients will be present. The bending associated with such gradients should lead to, or enhance, downdip extension in the cold upper half of the slab. In prominent western Pacific slabs, such as Tonga, Japan and Kuriles, slabs do not seem to develop any flattening at intermediate depths. In such regions, earthquake orientations in the slab mantle are largely explicable by a simple process of unbending (Wang, 2002).

9. Conclusions

Flat slab settings, though atypical, provide valuable insights into the relationship between slab geometry and intermediate depth seismicity. This study describes two regions where the pattern of flat slab seismicity varies systematically with slab curvature gradient. We argue that this relationship may arise through three important aspects of the dynamics: 1) the advective component of the slab bending rate is a dominant part of the long-term slab deformation rate; 2) pervasive inelastic deformation means that slabs only support elastic strain accumulation over short time/length scales compared to the duration of bending; 3) slabs are seismogenic only at temperatures below about 600 °C. In simultaneously describing aspects of both the distribution and orientation of slab earthquakes, this framework provides an important advance on existing models for the source of earthquake-producing stress. An important implication of the framework we present is that zones dominated by DT seismicity do not necessarily imply that slabs are in a state of uniform tension/stretching.

Acknowledgements

This work was supported by the Australian Research Council (Discovery grant DP150102887). Development of the Underworld2 code (<http://www.underworldcode.org/>) was supported by AuScope. DS's postgraduate research at the University of Melbourne was supported by a Baragwanath Geology Research Scholarship. This work was supported by resources provided by The Pawsey Supercomputing Centre with funding from the Australian Government and the Government of Western Australia. This work was supported by the Nectar Research Cloud, a collaborative Australian research platform supported by the National Collaborative Research Infrastructure Strategy (NCRIS). We thank Claire Currie for the careful review of this manuscript, and Gideon Rosenbaum for

providing important feedback on an early draft of this manuscript. The study benefited from discussions with Greg Houseman and Rebecca Farrington.

Appendix A. Identification of megathrust earthquakes

An event is assumed to be a megathrust rupture if it has a recorded depth of less than 70 km, the hypocenter lies within 20 km of the Slab2 surface model and the moment tensor exhibits strong similarity to a characteristic megathrust rupture along the local part of the trench. The window of 20 km is slightly larger than the typical depth errors of earthquakes located with depth phases (Engdahl et al., 1998). However, the difficulty of separating depth phases for shallow events, is relevant for the depth accuracy of earthquakes on the megathrust (Engdahl et al., 1998), which motivates the use of a larger window.

We use the trench azimuth to define the strike and rake of the reference megathrust rupture tensor (\mathbf{M}^{ref}), assuming a pure double-couple mechanism. The dip is set to a constant value of 20°. The similarity (χ) of a given earthquake (\mathbf{M}^k) is measured using the tensor dot product ($:$) of the normalised moment tensors:

$$\chi = \left[\frac{\mathbf{M}_{ij}^{\text{ref}} : \mathbf{M}_{ij}^k}{|\mathbf{M}^{\text{ref}}| |\mathbf{M}^k|} \right] \quad (\text{A.1})$$

We identified probable megathrust events using a focal mechanism similarity condition of $\chi \geq 0.75$. Additionally, all events which are greater than 20 km above the Slab2 were assumed to be upper plate events and not included in the analysis.

Fig. A.10 shows the events identified as megathrust ruptures for the MFS and PFS flat slab regions. In Mexico there are 106 events. If we use a smaller window, meaning that megathrust events must lie within 10 km of the Slab2 surface model, 83% of the events are retained. In Peru, there are only 26 megathrust events (even though the width of the domain is slightly wider). Using a 10 km window, 93% percent of these events are retained.

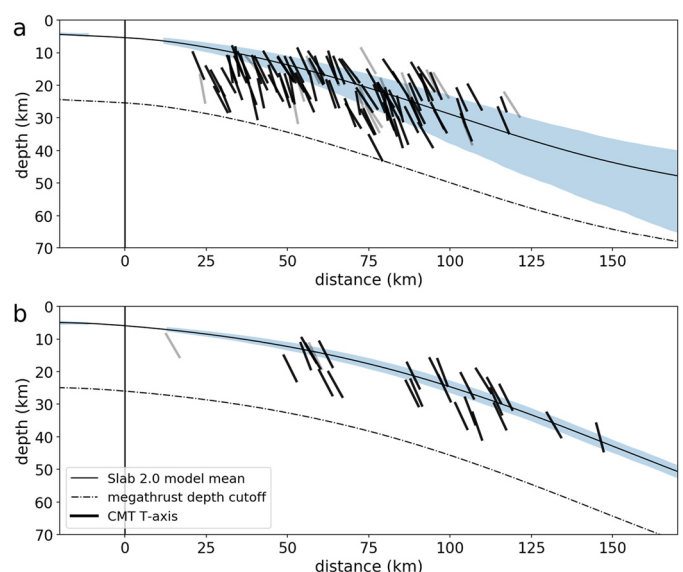


Fig. A.10. Megathrust earthquake identification. Projection of CMT T-axes on a vertical cross-section. Solid black lines show the region-averaged Slab2 model, as used in the geometric analysis. The blue strip shows the extent of variation in the S2 model, across the domain. a) Earthquakes identified as megathrust ruptures in the Mexican flat slab region. b) Same for Peru flat slab region.

Appendix B. Governing equations, numerical model and physical parameters

B.1. Continuity, momentum and energy equations

On geological time scales the Earth's mantle behaves as a highly viscous, incompressible fluid, in which inertial forces can be neglected. The flow caused by internal buoyancy anomalies is described by the static force-balance (momentum conservation) and continuity equations:

$$\sigma_{ij,j} + \rho g_i = 0 \quad (\text{B.1})$$

$$u_{i,i} = 0 \quad (\text{B.2})$$

where u_i is the i^{th} component of the velocity. Repeated indices denote summation, and $u_{,i}$ represents partial derivative with respect to the spatial coordinate x_i . The full stress tensor appearing in Eq. (B.1) can be decomposed into deviatoric and mean components:

$$\sigma_{ij} = \tau_{ij} + p\delta_{ij} \quad (\text{B.3})$$

It is noted that sign of the pressure (p) is opposite to the mean stress tensor, consistent with the convention that fluid flows from high to low pressure. The deviatoric stress tensor (τ) and the strain rate tensor (D_{ij}) are related according to the constitutive relationship:

$$\tau_{ij} = 2\eta D_{ij} = \eta(u_{i,j} + u_{j,i}) \quad (\text{B.4})$$

Substituting Eqs. (B.4) & (B.3) into Eq. (B.1) gives the Stokes equation, which involves two unknown variables: pressure, and velocity. The Stokes and continuity equation are sufficient to solve for the two unknowns, together with appropriate boundary conditions. An approximate solution to these equations is derived using a Galerkin Finite Element method, implemented in the *Underworld2* code (<http://www.underworldcode.org/>).

The thermal evolution of the system expresses the balance between heat transport by fluid motion, thermal diffusion and internal heat generation by the 1st Law of Thermodynamics, assuming incompressibility:

$$\rho C_p \frac{DT}{Dt} = q_{i,i} + \rho Q \quad (\text{B.5})$$

where T is the temperature and Q is the heat production rate (everywhere zero in this study). Diffusion rates are described by Fourier's Law, which satisfies the 2nd Law for positive conductivity (k):

$$q_i = -kT_{,i} \quad (\text{B.6})$$

Inserting Eq. (B.6) into Eq. (B.5), and using the definition of the material derivative gives:

$$\frac{\partial T}{\partial t} + u_i T_{,i} = (\kappa T_{,i})_{,i} + \frac{Q}{C_p} \quad (\text{B.7})$$

where $\kappa = \frac{k}{\rho C_p}$ is the thermal diffusivity.

The thermal variations are coupled to the momentum equation through their effect on density. At pressures in planetary interiors, silicate minerals are weakly compressible and this is generally considered as a perturbation to an incompressible flow. The Boussinesq approximation accounts for the buoyancy forces while neglecting the associated volume change allowing us to assume incompressibility (Eq. (B.2)). In the case of density variations due to temperature, the equation of state is:

$$\rho = \rho_0(1 - \alpha(T - T_p)) \quad (\text{B.8})$$

where ρ_0 is the density at a reference temperature (here the mantle potential temperature T_p). α is the coefficient of thermal expansion. It is generally much smaller than one, making the Boussinesq approximation reasonable.

The equations and parameters used in the numerical model are based on equivalent dimensionless forms of the governing equations. We use the following characteristic scales (e.g. Christensen, 1984):

$$\begin{aligned} \bar{x}_i &= x_i \left[\frac{1}{d} \right], \quad \bar{u}_i = u_i \left[\frac{d}{\kappa} \right], \quad \bar{\eta} = \eta \left[\frac{1}{\eta_0} \right], \\ \bar{\tau} &= \tau \left[\frac{d^2}{\kappa \eta_0} \right], \quad \bar{t} = t \left[\frac{\kappa}{d^2} \right], \quad \bar{T} = T \left[\frac{1}{\Delta T} \right] \end{aligned} \quad (\text{B.9})$$

where d is the mantle depth, t is time, η_0 is the reference viscosity and $\Delta T = (T_s - T_p)$, is the superadiabatic temperature difference across the fluid layer. Substituting dimensional terms for scaled dimensionless values (e.g. $x \rightarrow \bar{x}d$), and rearranging allows us to write the Stokes equation as:

$$2\bar{\eta}\bar{D}_{ij,j} + \bar{p}_{,i} = Ra(1 - \bar{T})(-\delta_{iz}) \quad (\text{B.10})$$

Overbars in Eq. (B.10) represent dimensionless quantities, and all dimensional parameters are contained in the dimensionless ratio Ra , the Rayleigh number which can be interpreted as a ratio of advection and diffusion timescales:

$$Ra = \frac{\rho_0 g \alpha \Delta T d^3}{\eta_0 \kappa} \quad (\text{B.11})$$

The dimensionless viscosity, which has a functional dependence on the total pressure, the temperature and the second invariant of the stress tensor, are described below.

The dimensionless form of the heat conservation equation is:

$$\frac{\partial \bar{T}}{\partial \bar{t}} + \bar{u}_i \bar{T}_{,i} = (\bar{T}_{,i})_{,i} + \bar{Q} \quad (\text{B.12})$$

where the dimensionless internal heating is given by:

$$\bar{Q} = Q \left[\frac{d^2}{\kappa C_p \Delta T} \right] \quad (\text{B.13})$$

B.2. Numerical method and model boundary conditions

The numerical model evolves according the simplified conservation equations for mass, momentum and energy described in B.2. Approximate solutions to the incompressible momentum and energy conservation equations are derived using the finite element code *Underworld 2* (<http://www.underworldcode.org/>). *Underworld2* is a Python API (Application Programming Interface) which provides functionality for the modelling of geodynamic processes. *Underworld2* solves the Stokes system through the standard mixed Galerkin finite element formulation. The 2D Cartesian domain is 1250 km in the vertical direction and has an aspect ratio of 4. The domain is partitioned into quadrilateral elements, with linear elements for velocity and constant elements for pressure (Q_1/dP_0). The mesh has 192 elements in the vertical direction, refined to provide an element width of ~ 2 km at the surface. Material properties are advected on Lagrangian tracer particles, with 50 tracers per element. During quadrature, material properties are mapped to quadrature points using nearest-neighbour interpolation. The Lagrangian tracer particles are used, primarily, to distinguish the subduction interface from the mantle and plates. *Underworld2* solves the energy conservation equation (advection-diffusion equation) using an explicit Streamline Upwind Petrov

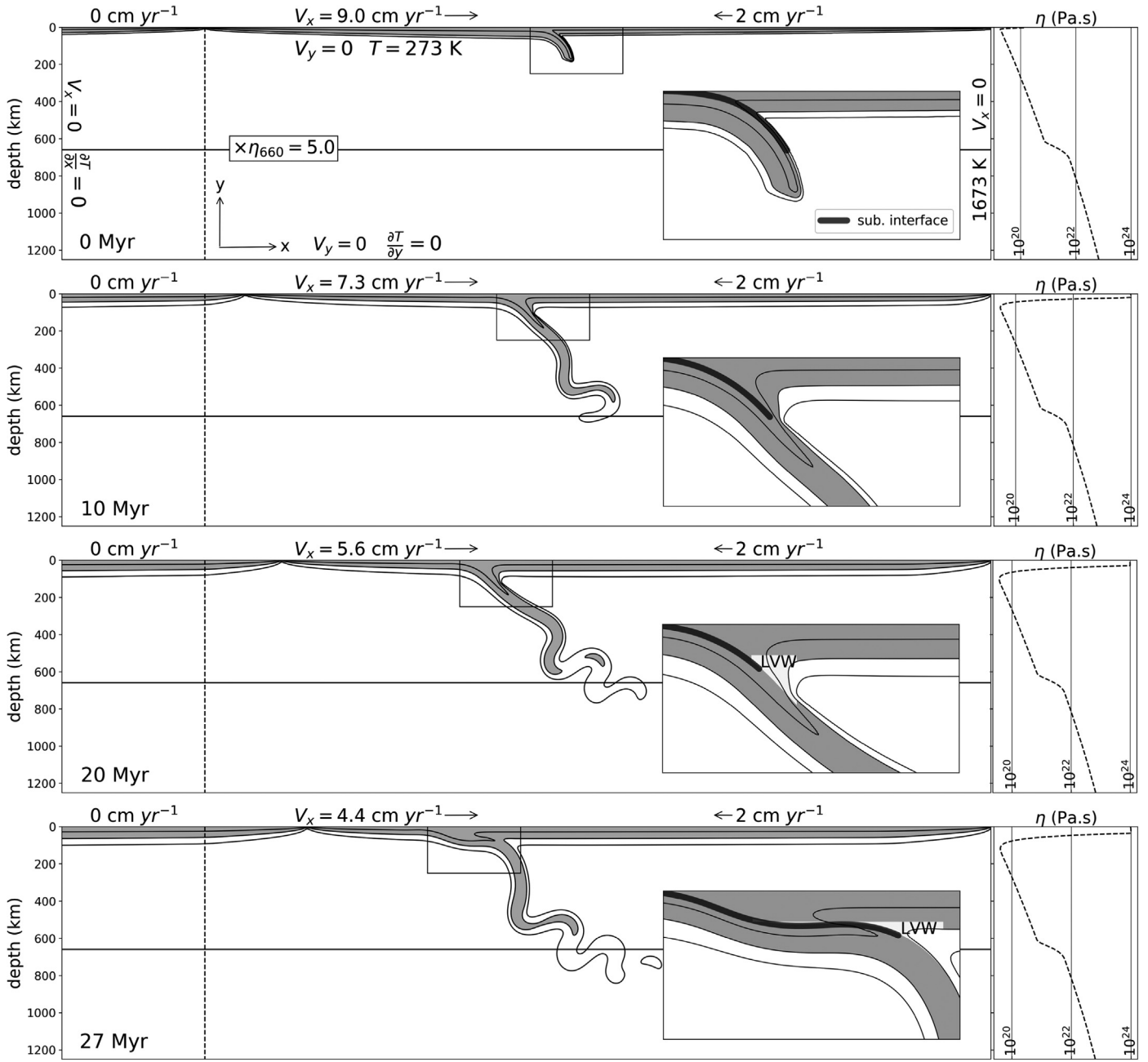


Fig. B.11. Model setup & evolution. The main panels show the full computational domain, with a binary colourmap applied to the temperature field at 1100 °C to delineate the location and evolution of the slab. Inset panels show subduction zone, including the position and depth of the subduction interface (dark grey) and the low viscosity wedge (labelled white region). Left hand panels show vertical viscosity profile evaluated along the vertical line in main panel, which coincides with the initial location of the ridge.

Galerkin (SUPG) method. In this approach, a Petrov-Galerkin formulation is obtained by using a modified weighting function which affects upwinding-type behaviour.

The model initial conditions comprise three plates and a small slab which follows a circular arc with a curvature radius of 200 km, truncated at 150 km depth. An overview of the model domain, initial conditions and evolving boundary conditions is shown in Fig. B.11. Previous studies have demonstrated that an imposed low viscosity mantle wedge (LVW) can cause slabs to flatten directly beneath the upper plate (Manea and Gurnis, 2007). We adopt a similar LVW strategy in this study, with further details of provided in the next section.

The Stokes system has free-slip conditions on the side and bottom boundaries. On the top boundary, $V_y = 0$, while constant boundary conditions on V_x are applied in a piece-wise fashion within the plate interiors. Plate interiors are defined by excluding a 150 km region either side of the subduction zone, and a 25 km region either side of the moving ridge). For the remaining nodes (i.e. near the plate boundaries) V_x is unconstrained. Plate velocities are prescribed based on a simplified model of the Cocos/NAM plate motion history. The applied horizontal velocity of the subducting plate (V_x) varies throughout the simulation, as shown in Fig. B.11. The velocity magnitude is 9 cm yr⁻¹ at the beginning of the model, decreasing linearly by a factor of 3 over the model duration (3 cm yr⁻¹ at 35 Myr). The upper plate retreat velocity

is constant at 2 cm yr^{-1} (toward the left hand side of the model domain). The ridge migrates at constant velocity of 2.0 cm yr^{-1} towards the trench (toward the right hand side of the domain), reflecting the migration of the Cocos/Pacific boundary. The energy equation has constant (Dirichlet) and zero-flux (Neumann), on the top and bottom boundary respectively. The right hand sidewall has a constant (potential) temperature which enforces a ridge at that boundary. The left sidewall has zero-flux. The potential temperature of the mantle is 1673 K, and the surface temperature is 273 K.

In the numerical model the mantle is treated as an incompressible, highly viscous fluid in which inertial forces and elastic stresses can be neglected. Thermal buoyancy helps to drive the flow in the model. The thermal variations are coupled to the momentum equation through their effect on density as well as through the temperature-dependent viscous rheology. A full description of the rheological formulation and physical parameter values are given in B.3. Following the approach of Manea and Gurnis (2007) the model incorporates a LVW that lies between two arbitrary depths (45 km & 150 km), the top of the slab, and a vertical line given by the intersection between the slab top and lower depth limit. The wedge viscosity is $2 \times 10^{20} \text{ Pa s}$, similar to the viscosity of the asthenospheric mantle in the model, but much weaker than the stagnant part of the mantle wedge that typically develops due to the strong temperature dependence of the mantle rheology (i.e. the cold corner). To generate an established convergent margin, we allowed an initial stage of subduction to proceed for 20 Myr, after which the LVW was imposed.

B.3. Rheology and model parameters

Mantle silicates deform through a range of mechanisms. At high temperatures, either diffusion creep (low stress) or dislocation creep (high stress) dominates (Karato and Wu, 1993). In addition to high-temperature creep, some form of stress limiting behaviour is expected to occur at low temperature, and high-stress. To keep the models as simple as possible we include two deformation mechanisms: grainsize-independent diffusion creep and a plastic yielding based on a truncated Drucker-Prager plasticity model. The viscosity associated with each deformation mechanism is combined using a harmonic average, denoted by η_c . The entire computational domain, except for the subduction interface, is governed by the same composite rheology: there is no compositional distinction between the mantle and plates.

Ductile flow laws for silicates often have an Arrhenius temperature and pressure dependence, controlled by the activation energy E , and activation volume V (Hirth and Kohlstedt, 2003). Additional dependencies, such as grain size and melt fraction, are neglected in this study, resulting in the following diffusion viscosity:

$$\eta_d = A \exp\left(\frac{E + p_l V}{RT_a}\right) \quad (\text{B.14})$$

where p_l indicates the lithostatic component of the pressure, and A is a constant. A linearised adiabatic term is added to the dimensionless temperature field, whenever it appears in an Arrhenius law:

$$T_a = T + z \times T_{,z}$$

$$T_{,z} = \frac{-\alpha g T_p}{C_p}$$

The dimensionless form of the creep law applied in the models uses the following scalings:

$$\bar{E} = E \left[\frac{1}{R \Delta T} \right], \quad \bar{W} = V \left[\frac{\rho_0 g d}{R \Delta T} \right], \quad \bar{A} = A \left[\frac{1}{\eta_0} \right] \quad (\text{B.15})$$

Note that $V \rightarrow \bar{W}$ includes a change from pressure dependence (dimensional) to depth dependence (dimensionless): The dimensionless diffusion creep viscosity can be written:

$$\bar{\eta}_d = \bar{A} \exp\left(\frac{\bar{E} + \bar{z} \bar{W}}{\bar{T}_s + \bar{T}_a}\right) \quad (\text{B.16})$$

where \bar{z} is the dimensionless depth and \bar{T}_s is the dimensionless surface temperature. The dimensionless linearised adiabatic component is incorporated as follows:

$$\bar{T}_a = \bar{T} + \bar{z} \times \bar{T}_{,z}$$

$$\bar{T}_{,z} = T_{,z} \left[\frac{d}{\Delta T} \right]$$

The parameters chosen for the diffusion creep law are similar to those used in previous studies utilising a composite linear-viscous and plastic formulation (Agrusta et al., 2017). A viscosity increase ($\times \eta_{660} = 5$) is applied at the 660 km discontinuity. As shown in Fig. B.11 the viscosity of the lower mantle at the bottom domain is about 50 times higher than the asthenosphere beneath the ridge, consistent with inferred values (Becker, 2017). The increase in viscosity is a combined effect of the prescribed viscosity jump and the effect of the pressure increase.

A range of pseudo-brittle and plastic deformation mechanisms can be approximated in the fluid constitutive model by allowing non-linearity in the viscosity ($\eta = \eta(T, p, J_I, \dots)$). The rheological model itself should be defined independently of the coordinate system, so it is necessary to define the constitutive model in terms of stress invariants (J_I). The viscoplastic approach defines an effective plastic viscosity η_p such that the deviatoric stress tensor is bounded by a yield stress τ_y :

$$\tau_y = 2\eta_p D_{ij} \quad (\text{B.17})$$

Assuming that η_p is isotropic and scalar (i.e. eigenvectors of the strain-rate tensor and deviatoric stress are identical), one can use the magnitude of both sides to define the scalar effective plastic viscosity as:

$$\eta_p = \frac{\tau_{y(\text{II})}}{2\epsilon_{\text{II}}} \quad (\text{B.18})$$

where the subscript II, denotes the square root of the tensor second invariant.

The yield stress function in the computational models is a truncated Drucker-Prager criterion:

$$\tau_y = \min(\tau_{\text{max}}, \mu p + C) \quad (\text{B.19})$$

where μ is the friction coefficient, and C is the cohesion. The Drucker-Prager yield surface is defined by the full pressure p . Because the pressure that appears in the dimensionless Stokes equation (Eq. (B.10)) is a dynamic pressure (\bar{p}), due to density variations only, the lithostatic pressure (a function of vertical coordinate) also needs to be accounted for. The dimensionless form of the yield stress is given by

$$\bar{\tau}_y = \min(\bar{\tau}_{\text{max}}, \bar{\mu}(\bar{p} + \bar{p}_l \bar{z}) + \bar{C}) \quad (\text{B.20})$$

where

$$\bar{\mu} = \mu,$$

$$\bar{C} = C \left[\frac{d^2}{\kappa \eta_0} \right],$$

$$\bar{\tau}_{\text{max}} = \tau_{\text{max}} \left[\frac{d^2}{\kappa \eta_0} \right],$$

$$\bar{p}_l = \bar{z} \left[\frac{\rho_0 g d^3}{\kappa \eta_0} \right]. \quad (\text{B.21})$$

The effective plastic viscosity (dimensionless) is given by

$$\bar{\eta}_p = \frac{\bar{\tau}_{y(II)}}{2\dot{\epsilon}_{II}} \quad (\text{B.22})$$

The final (composite) viscosity is the harmonic average of the viscosity associated with creep and plastic yielding:

$$\bar{\eta}_c = \frac{\bar{\eta}_d \bar{\eta}_p}{\bar{\eta}_d + \bar{\eta}_p} \quad (\text{B.23})$$

B.4. Model parameters and scaling values

This section provides a record of model parameters and reference values that are used in the models (see Tables B.1, B.2). In the numerical model, the dimensional parameters are non-dimensionalised using the scaling system described in this previous section and reference values provided in Table B.1.

Table B.1
Reference values used to non-dimensionalise the Stokes and Energy equations.

Reference value	Value	Symbol	Units
Length	2900	d	km
Viscosity	1×10^{20}	η_0	Pa s
Density	3300	ρ_0	kg m ⁻³
Thermal diffusivity	1×10^{-6}	κ	m ² s ⁻¹
Gravity	9.8	g	m s ⁻²
Temperature	1400	ΔT	K
Gas constant	8.314	R	J mol ⁻¹ K ⁻¹
Rayleigh number	3.31×10^8	Ra	–

Table B.2
Dimensional model parameters: †: Drucker-Prager, ‡: Low Viscosity Wedge. Model element resolution was 960×192 .

Parameter name	Value	Symbol	Units
Domain depth	1250	–	km
Domain width	5000	–	km
Potential temp	1673	T_p	K
Surface temp	273	T_s	K
Viscosity min.	1×10^{18}	–	Pa s
Viscosity max.	1×10^{24}	–	Pa s
Activation volume	5.3×10^{-6}	V	m ³ mol ⁻¹
Activation energy	320	E	kJ mol ⁻¹
Diffusion creep constant	6.3×10^{-10}	A	Pa ⁻¹ s ⁻¹
DP [†] friction coefficient	0.1	μ	–
DP cohesion	20	C	MPa
Yield stress max.	100	τ_{\max}	MPa
Sub. interface max thickness	14	W_{\max}	km
Sub. interface init/min thickness	7	W_{\min}	km
Sub. interface viscosity	9×10^{18}	–	Pa s
Sub. interface depth taper start	70	–	km
Sub. interface depth taper width	30	–	km
LVW [‡] viscosity	2×10^{20}	–	Pa s
LVW upper depth	45	–	km
LVW lower depth	150	–	km
Slab initial age at trench	20	–	Myr
Slab radius of curv.	200	–	km
Initial slab depth	150	–	km
Upper plate initial age at trench	10	–	Myr
Lower mantle viscosity increase	5	$\times \eta_{660}$	–
Adiabatic temp. gradient	3.7×10^{-4}	–	K m ⁻¹

References

Agrusta, R., Goes, S., van Hunen, J., 2017. Subducting-slab transition-zone interaction: stagnation, penetration and mode switches. *Earth Planet. Sci. Lett.* 464, 10–23. <https://doi.org/10.1016/j.epsl.2017.02.005>.

Bailey, I.W., Becker, T.W., Ben-Zion, Y., 2009. Patterns of co-seismic strain computed from southern California focal mechanisms. *Geophys. J. Int.* 177 (3), 1015–1036. <https://doi.org/10.1111/j.1365-246x.2009.04090.x>.

Becker, T.W., 2017. Superweak asthenosphere in light of upper mantle seismic anisotropy. *Geochem. Geophys. Geosyst.* 18 (5), 1986–2003. <https://doi.org/10.1002/2017gc006886>.

Billen, M.I., 2005. Constraints on subducting plate strength within the Kermadec trench. *J. Geophys. Res.* 110 (B5). <https://doi.org/10.1029/2004jb003308>.

Bishop, B.T., Beck, S.L., Zandt, G., Wagner, L., Long, M., Antonijevic, S.K., Kumar, A., Tavera, H., 2017. Causes and consequences of flat-slab subduction in southern Peru. *Geosphere* 13 (5), 1392–1407. <https://doi.org/10.1130/ges01440.1>.

Brudzinski, M.R., Thurber, C.H., Hacker, B.R., Engdahl, E.R., 2007. Global prevalence of double benioff zones. *Science* 316 (5830), 1472–1474. <https://doi.org/10.1126/science.1139204>.

Buffett, B.A., Becker, T.W., 2012. Bending stress and dissipation in subducted lithosphere. *J. Geophys. Res.* 117 (B5). <https://doi.org/10.1029/2012jb009205>.

Chen, P.-F., Bina, C.R., Okal, E.A., 2004. A global survey of stress orientations in subducting slabs as revealed by intermediate-depth earthquakes. *Geophys. J. Int.* 159 (2), 721–733. <https://doi.org/10.1111/j.1365-246x.2004.02450.x>.

Christensen, U., 1984. Convection with pressure- and temperature-dependent non-Newtonian rheology. *Geophys. J. Int.* 77 (2), 343–384. <https://doi.org/10.1111/j.1365-246x.1984.tb01939.x>.

Comte, D., Suarez, G., 1994. An inverted double seismic zone in Chile: evidence of phase transformation in the subducted slab. *Science* 263 (5144), 212–215. <https://doi.org/10.1126/science.263.5144.212>.

Comte, D., Dörmath, L., Pardo, M., Monfret, T., Haessler, H., Rivera, L., Frogneux, M., Glass, B., Meneses, C., 1999. A double-layered seismic zone in Arica, northern Chile. *Geophys. Res. Lett.* 26 (13), 1965–1968. <https://doi.org/10.1029/1999gl900447>.

Craig, T.J., 2019. Accurate depth determination for moderate-magnitude earthquakes using global teleseismic data. *J. Geophys. Res., Solid Earth* 124 (2), 1759–1780. <https://doi.org/10.1029/2018jb016902>.

Ekström, G., Nettles, M., Dziewoński, A., 2012. The global CMT project 2004–2010: centroid-moment tensors for 13,017 earthquakes. *Phys. Earth Planet. Inter.* 200–201, 1–9. <https://doi.org/10.1016/j.pepi.2012.04.002>.

Engdahl, E.R., Scholz, C.H., 1977. A double benioff zone beneath the central Aleutians: an unbending of the lithosphere. *Geophys. Res. Lett.* 4 (10), 473–476. <https://doi.org/10.1029/gl004i010p00473>.

Engdahl, E.R., van der Hilst, R., Buland, R., 1998. Global teleseismic earthquake relocation with improved travel times and procedures for depth determination. *Bull. Seismol. Soc. Am.* 88 (3), 722–743.

England, P., Engdahl, R., Thatcher, W., 2004. Systematic variation in the depths of slabs beneath arc volcanoes. *Geophys. J. Int.* 156 (2), 377–408. <https://doi.org/10.1111/j.1365-246x.2003.02132.x>.

Ferrari, L., Orozco-Esquivel, T., Manea, V., Manea, M., 2012. The dynamic history of the trans-Mexican volcanic belt and the Mexico subduction zone. *Tectonophysics* 522–523, 122–149. <https://doi.org/10.1016/j.tecto.2011.09.018>.

Florez, M.A., Prieto, G.A., 2019. Controlling factors of seismicity and geometry in double seismic zones. *Geophys. Res. Lett.* 46 (8), 4174–4181. <https://doi.org/10.1029/2018gl081168>.

Forsyth, D., Uyeda, S., 1975. On the relative importance of the driving forces of plate motion. *Geophys. J. Int.* 43 (1), 163–200. <https://doi.org/10.1111/j.1365-246x.1975.tb00631.x>.

Fujita, K., Kanamori, H., 1981. Double seismic zones and stresses of intermediate depth earthquakes. *Geophys. J. Int.* 66 (1), 131–156. <https://doi.org/10.1111/j.1365-246x.1981.tb05950.x>.

Hacker, B.R., Peacock, S.M., Abers, G.A., Holloway, S.D., 2003. Subduction factory 2. are intermediate-depth earthquakes in subducting slabs linked to metamorphic dehydration reactions? *J. Geophys. Res., Solid Earth* 108 (B1). <https://doi.org/10.1029/2001jb001129>.

Hayes, G.P., Moore, G.L., Portner, D.E., Hearne, M., Flamme, H., Furtney, M., Smoczyk, G.M., 2018. Slab2, a comprehensive subduction zone geometry model. *Science* 362 (6410), 58–61. <https://doi.org/10.1126/science.aat4723>.

Hirth, G., Kohlstedt, D., 2003. Rheology of the upper mantle and the mantle wedge: a view from the experimentalists. In: *Inside the Subduction Factory*. American Geophysical Union, pp. 83–105.

House, L.S., Jacob, K.H., 1982. Thermal stresses in subducting lithosphere can explain double seismic zones. *Nature* 295 (5850), 587–589. <https://doi.org/10.1038/295587a0>.

Isacks, B., Molnar, P., 1969. Mantle earthquake mechanisms and the sinking of the lithosphere. *Nature* 223 (5211), 1121–1124. <https://doi.org/10.1038/2231121a0>.

Isacks, B., Molnar, P., 1971. Distribution of stresses in the descending lithosphere from a global survey of focal-mechanism solutions of mantle earthquakes. *Rev. Geophys.* 9 (1), 103. <https://doi.org/10.1029/rg009i001p0103>.

Jackson, J., 1980. Errors in focal depth determination and the depth of seismicity in Iran and Turkey. *Geophys. J. Int.* 61 (2), 285–301. <https://doi.org/10.1111/j.1365-246x.1980.tb04318.x>.

Karato, S.I., Wu, P., 1993. Rheology of the upper mantle: a synthesis. *Science* 260 (5109), 771–778. <https://doi.org/10.1126/science.260.5109.771>.

Kawakatsu, H., 1986. Double seismic zones: kinematics. *J. Geophys. Res.* 91 (B5), 4811. <https://doi.org/10.1029/jb091i05p04811>.

Kim, Y., Clayton, R.W., Asimow, P.D., Jackson, J.M., 2013. Generation of talc in the mantle wedge and its role in subduction dynamics in central Mexico. *Earth Planet. Sci. Lett.* 384, 81–87. <https://doi.org/10.1016/j.epsl.2013.10.006>.

- Kirby, S., Engdahl, R.E., Denlinger, R., 2013. Intermediate-depth intraslab earthquakes and arc volcanism as physical expressions of crustal and uppermost mantle metamorphism in subducting slabs. In: *Subduction Top to Bottom*. American Geophysical Union, pp. 195–214.
- Kita, S., Katsumata, K., 2015. Stress drops for intermediate-depth intraslab earthquakes beneath Hokkaido, northern Japan: differences between the subducting oceanic crust and mantle events. *Geochem. Geophys. Geosyst.* 16 (2), 552–562. <https://doi.org/10.1002/2014gc005603>.
- Kumar, A., Wagner, L.S., Beck, S.L., Long, M.D., Zandt, G., Young, B., Tavera, H., Minaya, E., 2016. Seismicity and state of stress in the central and southern Peruvian flat slab. *Earth Planet. Sci. Lett.* 441, 71–80. <https://doi.org/10.1016/j.epsl.2016.02.023>.
- Lemoine, A., Madariaga, R., Campos, J., 2002. Slab-pull and slab-push earthquakes in the Mexican, Chilean and Peruvian subduction zones. *Phys. Earth Planet. Inter.* 132 (1–3), 157–175. [https://doi.org/10.1016/S0031-9201\(02\)00050-X](https://doi.org/10.1016/S0031-9201(02)00050-X).
- Manea, V., Gurnis, M., 2007. Subduction zone evolution and low viscosity wedges and channels. *Earth Planet. Sci. Lett.* 264 (1–2), 22–45. <https://doi.org/10.1016/j.epsl.2007.08.030>.
- Manea, V., Manea, M., Ferrari, L., 2013. A geodynamical perspective on the subduction of Cocos and Rivera plates beneath Mexico and central America. *Tectonophysics* 609, 56–81. <https://doi.org/10.1016/j.tecto.2012.12.039>.
- Manea, V., Manea, M., Ferrari, L., Orozco-Esquivel, T., Valenzuela, R., Husker, A., Kostoglodov, V., 2017. A review of the geodynamic evolution of flat slab subduction in Mexico, Peru, and Chile. *Tectonophysics* 695, 27–52. <https://doi.org/10.1016/j.tecto.2016.11.037>.
- McAdoo, D.C., Caldwell, J.G., Turcotte, D.L., 1978. On the elastic-perfectly plastic bending of the lithosphere under generalized loading with application to the Kuril trench. *Geophys. J. Int.* 54 (1), 11–26. <https://doi.org/10.1111/j.1365-246x.1978.tb06753.x>.
- McKenzie, D.P., 1969. Speculations on the consequences and causes of plate motions. *Geophys. J. Int.* 18 (1), 1–32. <https://doi.org/10.1111/j.1365-246x.1969.tb00259.x>.
- Melgar, D., Pérez-Campos, X., Ramírez-Guzmán, L., Spica, Z., Espíndola, V.H., Hammond, W.C., Cabral-Cano, E., 2018. Bend faulting at the edge of a flat slab: the 2017 Mw 7.1 Puebla-Morelos, Mexico earthquake. *Geophys. Res. Lett.* 45 (6), 2633–2641. <https://doi.org/10.1002/2017gl076895>.
- Myhill, R., 2012. Slab buckling and its effect on the distributions and focal mechanisms of deep-focus earthquakes. *Geophys. J. Int.* 192 (2), 837–853. <https://doi.org/10.1093/gji/ggs054>.
- Peacock, S.M., 2001. Are the lower planes of double seismic zones caused by serpentine dehydration in subducting oceanic mantle? *Geology* 29 (4), 299. [https://doi.org/10.1130/0091-7613\(2001\)029<0299:atlpod>2.0.co;2](https://doi.org/10.1130/0091-7613(2001)029<0299:atlpod>2.0.co;2).
- Ribe, N.M., 2001. Bending and stretching of thin viscous sheets. *J. Fluid Mech.* 433, 135–160. <https://doi.org/10.1017/S0022112000003360>.
- Sandiford, D., Moresi, L., 2019. Improving subduction interface implementation in dynamic numerical models. *Solid Earth* 10 (3), 969–985. <https://doi.org/10.5194/se-10-969-2019>.
- Schepers, G., van Hinsbergen, D.J.J., Spakman, W., Kesters, M.E., Boschman, L.M., McQuarrie, N., 2017. South-American plate advance and forced Andean trench retreat as drivers for transient flat subduction episodes. *Nat. Commun.* 8 (1). <https://doi.org/10.1038/ncomms15249>.
- Sleep, N.H., 1979. The double seismic zone in downgoing slabs and the viscosity of the mesosphere. *J. Geophys. Res.* 84 (B9), 4565. <https://doi.org/10.1029/jb084ib09p04565>.
- van Hunen, J., van den Berg, A.P., Vlaar, N.J., 2000. A thermo-mechanical model of horizontal subduction below an overriding plate. *Earth Planet. Sci. Lett.* 182 (2), 157–169. [https://doi.org/10.1016/S0012-821X\(00\)00240-5](https://doi.org/10.1016/S0012-821X(00)00240-5).
- Wang, K., 2002. Unbending combined with dehydration embrittlement as a cause for double and triple seismic zones. *Geophys. Res. Lett.* 29 (18), 36–1–36–4. <https://doi.org/10.1029/2002gl015441>.
- Wei, S.S., Wiens, D.A., van Keken, P.E., Cai, C., 2017. Slab temperature controls on the Tonga double seismic zone and slab mantle dehydration. *Sci. Adv.* 3 (1), e1601755. <https://doi.org/10.1126/sciadv.1601755>.
- Yamasaki, T., Seno, T., 2003. Double seismic zone and dehydration embrittlement of the subducting slab. *J. Geophys. Res., Solid Earth* 108 (B4). <https://doi.org/10.1029/2002jb001918>.